

# Sensor diaphragm under initial tension: Nonlinear responses and design implications

Miao Yu<sup>a</sup>, Xinhua Long<sup>b</sup>, B. Balachandran<sup>a,\*</sup>

<sup>a</sup>*Department of Mechanical Engineering, University of Maryland, College Park, MD 20742-3035, USA*

<sup>b</sup>*State Key Laboratory of Mechanical System and Vibration, Shanghai Jiao Tong University, Shanghai 200240, PR China*

Received 21 November 2005; received in revised form 29 June 2007; accepted 9 July 2007

---

## Abstract

In this article, recent investigations into the dynamic behavior of a pressure-sensor diaphragm under initial tension are presented. A comprehensive mechanics model based on a plate with in-plane tension is presented and linear analysis is carried out to examine the transition from plate behavior to membrane behavior. It is shown that, for certain tension parameter values, it is appropriate to model the diaphragm as a plate–membrane structure rather than as a membrane or a plate. In the nonlinear analysis, the effect of cubic nonlinearity on the response is studied when the excitation frequency is close to either one-third of the first natural frequency or the first natural frequency. The nonlinearity limits the sensor bandwidth and dynamic range. It is discussed as to how a high bandwidth and high sensitivity can be realized by decreasing the diaphragm thickness and applying an appropriate tension. However, as the in-plane tension is changed, there is a trade-off between the sensitivity and dynamic pressure range. The analyses and related results should be valuable for carrying out the design of circular diaphragms for various sensor applications, in particular, for designing sensors on small scales.

© 2007 Elsevier Ltd. All rights reserved.

---

## 1. Introduction

The diaphragm structure is a common element of different types of pressure sensors, including silicon piezoresistive sensors, capacitive sensors, and fiber-optic sensors [1–3]. When a diaphragm is used as a sensor transducer for dynamic pressure sensing, the vibration of this diaphragm structure is detected either through the displacement of the diaphragm or through the strain induced in the diaphragm by the vibration. In recent work [3–7], both of these two means have been considered for designing appropriate mechanical elements for fiber-optic pressure sensors. Since the sensitivity, bandwidth, and linearity of a pressure sensor are directly related to the structural behavior of the diaphragm, choosing an appropriate diaphragm model is important for optimizing the sensor design parameters and achieving an optimum sensor performance. In many cases, the diaphragm is a stretched thin structure such as in a condenser microphone, and the membrane equations

---

\*Corresponding author. Tel.: +1 301 405 5309; fax: +1 301 314 9477.

E-mail addresses: [balab@umd.edu](mailto:balab@umd.edu), [balab@eng.umd.edu](mailto:balab@eng.umd.edu) (B. Balachandran).

are usually used for analyzing the diaphragm vibrations [1–4]. However, as pointed out in the recent work of Yu and Balachandran [8], a membrane model is not always the most appropriate one.

Sheplak and Dugundji [9] carried out static analysis of a clamped circular plate under initial tension and studied the transition range from plate behavior to membrane behavior in terms of the tension parameter  $k$ . For “small” plate deflections, they have shown that the transition from plate behavior to membrane behavior can be described in terms of a non-dimensional tension parameter  $k$ . This transition occurs over the range  $1 < k < 20$ , with the plate behavior dominating for  $k < 1$  and the membrane behavior dominating for  $k > 20$ . In the work of Yu and Balachandran [8], this earlier work is extended to the dynamic case and the diaphragm response is characterized in terms of the tension parameter  $k$ . It is shown that the transition range depends on the vibration mode of interest. The authors also discussed how the analysis and related results can be used to tailor the sensor diaphragm characteristics to address the trade-off between sensitivity and bandwidth. In addition to the sensitivity and bandwidth, the dynamic range is another important sensor design parameter that needs to be investigated through a nonlinear analysis. In this paper, this is carried out to obtain a fundamental understanding of the effects of the nonlinearity on the pressure-sensor performance. In this regard, it is pointed out that the importance of considering the influence of the nonlinearity on the frequency response of a pressure sensor has been previously recognized [10]. However, the treatment presented here allows for a more complete examination of the influence of the nonlinearity since it is not restricted to be necessarily weak. This enables one to get a more complete picture of the sensor behavior.

The rest of this article is organized as follows. In Section 2, the model of a plate with in-plane tension is provided and the linear analysis conducted earlier is revisited. The plate–membrane transition behavior is discussed and the results obtained for a representative case are presented. In Section 3, the nonlinear analysis is detailed and results are presented for cases when the excitation frequency is close to the first natural frequency and one-third of the first natural frequency. The effects of the nonlinearity, initial tension, and damping on the sensor bandwidth and dynamic range are discussed along with guidelines for designing a pressure-sensor diaphragm. Concluding remarks are collected together in the last section.

## 2. Model development, linear analysis, and results

In Fig. 1, a clamped, circular diaphragm of radius  $a$  and thickness  $h$  subjected to a uniform pressure field  $p$  is illustrated. Young’s modulus of elasticity and Poisson’s ratio of the diaphragm material are denoted by  $E$  and  $\nu$ , respectively. The initial tension per unit length applied to the diaphragm is represented by  $N_0$ .

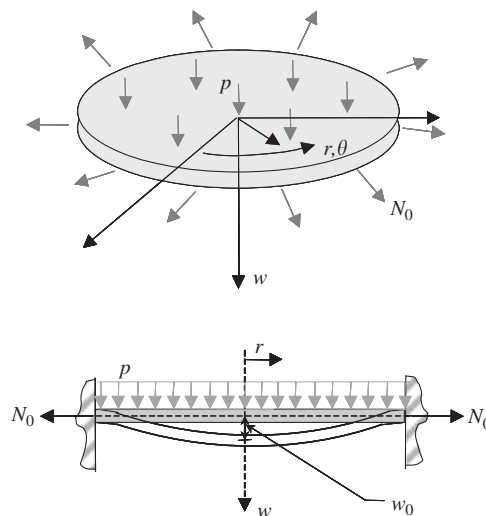


Fig. 1. Illustration of a diaphragm clamped along its edge.

The non-dimensional tension parameter  $k$  is defined by

$$k = a\sqrt{\frac{N_0}{D}} = \frac{a}{h}\sqrt{\frac{12(1-v^2)N_0/h}{E}} = \frac{a}{h}\sqrt{\frac{12(1-v^2)T}{E}}, \tag{1}$$

where the constant  $D = Eh^3/(12(1-v^2))$  and  $T = N_0/h$  is the tension per unit area. In the analysis that follows, it is shown the choice of a plate model or a membrane model actually depends on the tension parameter  $k$ , not on just the initial tension per unit length  $N_0$  applied to the diaphragm. The nonlinear partial-differential equation governing an isotropic plate with initial tension is of the form [11,12]

$$\begin{aligned} \rho h \frac{\partial^2 w}{\partial t^2} + D\nabla^4 w - N_0\nabla^2 w = & \frac{\partial^2 w}{\partial r^2} \left( \frac{1}{r} \frac{\partial \Phi}{\partial r} + \frac{1}{r^2} \frac{\partial^2 \Phi}{\partial \theta^2} \right) + \frac{\partial^2 \Phi}{\partial r^2} \left( \frac{1}{r} \frac{\partial w}{\partial r} + \frac{1}{r^2} \frac{\partial^2 w}{\partial \theta^2} \right) \\ & - 2 \left( \frac{1}{r} \frac{\partial^2 \Phi}{\partial r \partial \theta} - \frac{1}{r^2} \frac{\partial \Phi}{\partial \theta} \right) \left( \frac{1}{r} \frac{\partial^2 w}{\partial r \partial \theta} - \frac{1}{r^2} \frac{\partial w}{\partial \theta} \right) \\ & - 2\mu \frac{\partial w}{\partial t} + f(r, \theta; t), \end{aligned} \tag{2}$$

where  $r$  is the radial distance from the center,  $\theta$  is the angular coordinate,  $t$  is the time variable,  $w(r, \theta; t)$  is the transverse displacement,  $\mu$  is the damping coefficient, and  $f(r, \theta; t)$  is the transverse loading per unit area. As shown in Ref. [12], the stress function  $\Phi$  should satisfy the compatibility equation

$$\nabla^4 \Phi = Eh \left[ \left( \frac{1}{r} \frac{\partial^2 w}{\partial r \partial \theta} - \frac{1}{r^2} \frac{\partial w}{\partial \theta} \right)^2 - \frac{\partial^2 w}{\partial r^2} \left( \frac{1}{r} \frac{\partial w}{\partial r} + \frac{1}{r^2} \frac{\partial^2 w}{\partial \theta^2} \right) \right]. \tag{3}$$

The boundary conditions along the clamped edge at  $r = a$ , the requirement that the transverse displacement is finite at the plate center (i.e.,  $r = 0$ ), and the conditions on the radial displacement  $u$  and the hoop displacement  $v_h$  are given by

$$\begin{aligned} w(r, \theta; t)|_{r=a} = 0, \quad \left. \frac{\partial w(r, \theta; t)}{\partial r} \right|_{r=a} = 0, \quad u|_{r=a} = u_0 = \frac{N_0(1-v)a}{Eh}, \quad v_h|_{r=a} = 0, \\ \left| w(r, \theta; t) \right|_{r=0} < \infty, \quad \left| \Phi(r, \theta; t) \right|_{r=0} < \infty. \end{aligned} \tag{4}$$

From Eqs. (4) and (A.12)–(A.17) of Appendix A, one can obtain the following conditions on  $\Phi$ :

$$\frac{\partial^2 \Phi}{\partial r^2} - v \left( \frac{1}{r} \frac{\partial \Phi}{\partial r} + \frac{1}{r^2} \frac{\partial^2 \Phi}{\partial \theta^2} \right) = 0 \text{ at } r = a, \tag{5}$$

$$\frac{\partial^3 \Phi}{\partial r^3} + \frac{1}{r} \frac{\partial^2 \Phi}{\partial r^2} - \frac{1}{r^2} \frac{\partial \Phi}{\partial r} + \frac{2+v}{r^2} \frac{\partial^3 \Phi}{\partial r \partial \theta^2} - \frac{3+v}{r^3} \frac{\partial^2 \Phi}{\partial \theta^2} = 0 \text{ at } r = a. \tag{6}$$

For “small” transverse displacements, Eq. (2) can be reduced to the linear form [10–13]

$$\rho h \frac{\partial^2 w}{\partial t^2} + D\nabla^4 w - N_0\nabla^2 w = -2\mu \frac{\partial w}{\partial t} + f(r, \theta; t). \tag{7}$$

As discussed in the work of Yu and Balachandran [8], for the linear, undamped and unforced system, the characteristic equation is given by

$$I_m(\alpha_{1m}a)J'_m(\alpha_{2m}a) - J_m(\alpha_{2m}a)I'_m(\alpha_{1m}a) = 0, \tag{8}$$

where the prime indicates a derivative with respect to  $r$  and the functions  $I_m(\alpha_1 r)$  and  $J_m(\alpha_2 r)$  are the modified Bessel function of the first kind and the Bessel function of the first kind, respectively. Each of these functions is of order  $m$ , which is used as a vibration mode index along the circular direction. Determining the roots of Eq. (8) for each value of  $m$  and labeling them successively using the integer  $n$ , which is used as a vibration mode index along the radial direction, it is found that the natural frequencies can be written as

$$\omega_{mn}^2 = \frac{D}{\rho h a^4} (\alpha_{2mn} a)^2 [(\alpha_{2mn} a)^2 + k^2], \tag{9}$$

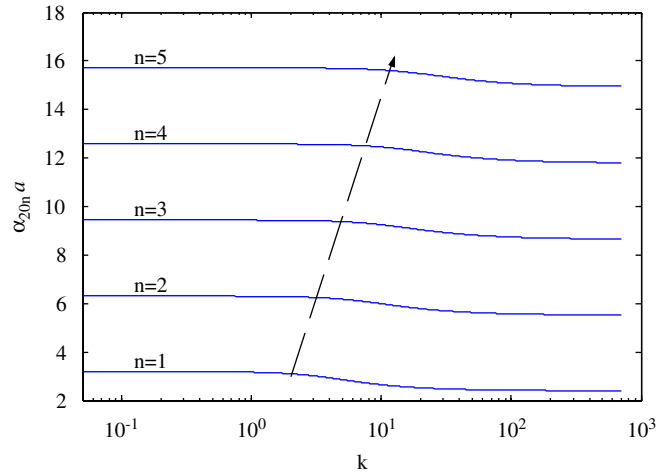


Fig. 2. Different vibration modes: transition behavior with respect to the tension parameter  $k$ .

where  $k$  is the tension parameter introduced in Eq. (1). The associated mode shapes are given by

$$W_{mn}(r, \theta) = A_{mn} \left[ J_m(\alpha_{2mn}r) - \frac{J_m(\alpha_{2mn}a)}{I_m(\alpha_{1mn}a)} I_m(\alpha_{1mn}r) \right] \cos m(\theta - \varphi_m). \quad (10)$$

In Fig. 2, for the first vibration mode (i.e.,  $m = 0$ ,  $n = 1$ ) and the other vibration modes, the transition from plate behavior to membrane behavior is shown. To obtain each of these plots, the eigenvalue ( $\alpha_{2mn}a$ ) is determined from Eq. (8) for different values of  $k$ . For the first vibration mode, as  $k$  decreases and takes on values less than 1, the graph of ( $\alpha_{2mn}a$ ) is asymptotic to the plate case (i.e.,  $\alpha_{201}a = 3.196$ ). As  $k$  increases and becomes larger than 20, the graph of ( $\alpha_{2mn}a$ ) is asymptotic to the membrane case (i.e.,  $\alpha_{201}a = 2.404$ ). There is a transition from a plate behavior to a membrane behavior in the region  $1 < k < 20$ . This result is similar to that obtained by Sheplak and Dugundji [9] for the static case. For higher vibration modes, this transition region also exists and it moves towards the direction of increasing  $k$ .

When designing a pressure sensor, the sensor bandwidth is chosen to be less than the first natural frequency of the diaphragm. As shown in Ref. [8], by either decreasing the radius, increasing the thickness, or increasing the tension parameter, the first natural frequency of the diaphragm can be increased, which in turn increases the sensor bandwidth. However, trade-offs that exist between the bandwidth and sensitivity have to be examined carefully, since a high bandwidth may not mean high sensitivity and vice versa. Assuming that the sensing mechanism is based on a pressure-induced diaphragm displacement measurement (in most cases, the diaphragm center displacement), the sensitivity is proportional to the diaphragm center displacement under unit pressure.

Considering the forced response of a damped diaphragm subjected to the harmonic excitation  $f(r, \theta; t) = p \cos \omega t$  and using a single-mode approximation, the diaphragm displacement at the center (i.e.,  $r = 0$ ) can be shown to be [8]

$$U_0(r = 0, \theta) = \frac{2\pi p a}{\rho h N_1} \frac{[(1/\alpha_{201})J_1(\alpha_{101}a) - (J_0(\alpha_{201}a)/\alpha_{101}I_0(\alpha_{101}a))I_1(\alpha_{101}a)] [1 - J_0(\alpha_{201}a)/I_0(\alpha_{101}a)]}{\omega_{01} \sqrt{[1 - (\omega/\omega_{01})^2]^2 + 4\zeta_1^2(\omega/\omega_{01})^2}}, \quad (11)$$

where

$$\zeta_1 = \frac{\mu}{\rho h \omega_{01}}, \quad N_1 = \frac{1}{A_{01}^2} \int_0^a 2\pi r W_{01}^2(r, \theta) dr,$$

$\omega_{01}$  is the natural frequency of the first vibration mode, and  $A_{01}$  is a constant associated with the first mode shape  $W_{01}(r, \theta)$ .

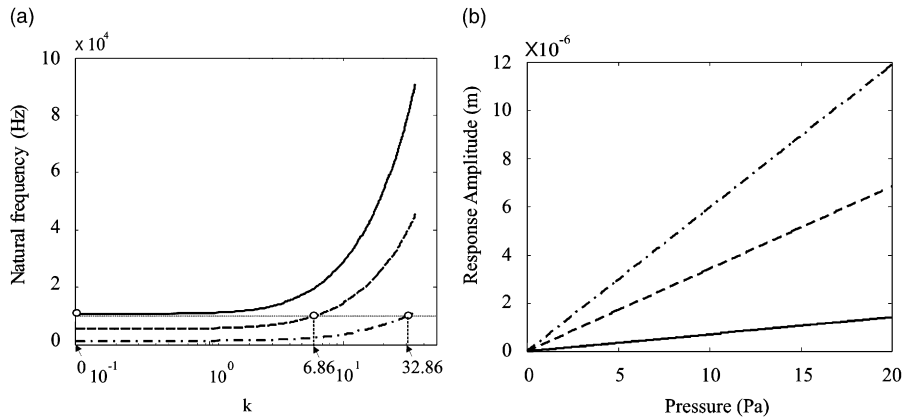


Fig. 3. (a) Variation of the first natural frequency with respect to the tension parameter for diaphragm structures with different thickness values, (—) for  $h = 40 \mu\text{m}$ , (----) for  $h = 20 \mu\text{m}$ , and (- · -) for  $h = 5 \mu\text{m}$ , respectively, and (b) variation of the diaphragm center displacement amplitude with respect to the excitation pressure for diaphragm structures with different tension parameter values but the same first natural frequency, (—) for  $k = 0$ , (----) for  $k = 6.86$ , and (- · -) for  $k = 32.86$ , respectively.

Table 1  
Structural system parameters and characteristics

Cases	$h$ ( $\mu\text{m}$ )	$a$ (mm)	$k$	$\omega_{01}$ (kHz)
1	40	1.75	0	10.97
2	20	1.75	6.86	10.97
3	5	1.75	32.86	10.97

As a representative case, a Mylar diaphragm with the Young’s modulus of elasticity  $E = 3.45 \times 10^9 \text{ Pa}$ , density  $\rho = 1.29 \times 10^3 \text{ kg/m}^3$ , and Poisson’s ratio  $\nu = 0.41$  is considered. For a diaphragm radius of 1.75 mm and thickness values of 40, 20 and 5  $\mu\text{m}$ , the dependence of the first natural frequency on the tension parameter  $k$  is shown for each of these cases in Fig. 3a. As expected from Eq. (9), the natural frequencies increase as the tension parameter  $k$  is increased. When the tension parameter  $k$  is less than 1; i.e., the plate behavior is dominant, the natural frequencies almost stay constant with respect to  $k$ . However, when  $k$  is larger than 20; i.e., the membrane behavior is dominant, the natural frequencies increase rapidly. Note that it is possible to get the same natural frequency (10.97 kHz) as that for the diaphragm with  $h = 40 \mu\text{m}$  and  $k = 0$  by choosing the appropriate tension parameters. As pointed out in Fig. 3a, the tension parameter values are  $k = 6.86$  and 32.86, for  $h = 20$  and 5  $\mu\text{m}$ , respectively. The structural and system parameters for the previously mentioned three diaphragm structures are presented in Table 1. Again, these parameters have been chosen so that the first natural frequency in each of the three cases is 10.97 kHz.

As discussed earlier, the sensitivity of a pressure sensor is related to ratio of the diaphragm center displacement to the magnitude of the pressure disturbance (slopes of the curves in Fig. 3b). The variation of the response amplitude of the diaphragm center with respect to pressure amplitude is shown in Fig. 3b for the three cases shown in Table 1. It can be seen that for the diaphragm with the lowest thickness value ( $h = 5 \mu\text{m}$ ) and highest tension parameter value ( $k = 32.86$ ), the corresponding curve in Fig. 3b has the largest slope, indicating the corresponding sensor has the highest sensitivity. These results show that it is possible to address the trade-off between sensitivity and bandwidth and realize a sensor with both high sensitivity and high bandwidth by reducing the diaphragm thickness and applying appropriate tension.

In the next section, the effect of the nonlinearity in Eq. (2) on the sensor response and performance characteristics is examined for diaphragms with and without initial tension.

### 3. Nonlinear analysis, results, and discussion

Starting from Eq. (2), first the following equation governing the axi-symmetric response is obtained:

$$\rho h \frac{\partial^2 w}{\partial t^2} + D \nabla^4 w - N_0 \nabla^2 w = \frac{1}{r} \frac{\partial}{\partial r} \left( r N_r \frac{\partial w}{\partial r} \right) - 2\mu \frac{\partial w}{\partial t} + f(r, \theta; t). \quad (12a)$$

Then, the following variables are introduced:

$$\begin{aligned} r &= ar^*, & t &= a^2 \sqrt{\frac{\rho h}{D}} t^*, & w &= \frac{h^2}{a} w^*, & \mu &= \frac{24(1-\nu^2)}{a^4} \sqrt{\rho h^5 D} \mu^*, \\ f &= \frac{D h^2}{a^5} f^*, & N_0 &= \frac{E h^5}{a^3} N_0^*, & \text{and } \Phi &= \frac{E h^5}{a^2} \Phi^*. \end{aligned} \quad (12b)$$

Next, dropping the asterisks from here onwards for the dimensionless quantities, the response in the axi-symmetric case is considered to be of the form

$$w(r, t; \varepsilon) = \sum_{m=1}^{\infty} \psi_m(t; \varepsilon) W_m(r), \quad (13)$$

where  $W_m(r)$  are the free-oscillation modes from the linear undamped problem and  $\varepsilon$  is a “small” dimensionless parameter. This parameter is defined as  $\varepsilon = 12(1-\nu^2)h^2/a^2$ , where  $h$  is the diaphragm thickness and  $a$  is the diaphragm radius. For a single-mode approximation (the first mode here), the temporal amplitude of the sensor diaphragm is governed by [5,11,12]

$$\ddot{\psi}_1 + \omega_1^2 \psi_1 = \varepsilon \left[ \Gamma_{1111} \psi_1^3 - 2\mu_1 \dot{\psi}_1 \right] + f_1(t), \quad (14)$$

where  $\omega_{01} = (\omega_1/a^2)\sqrt{D/\rho h}$  and the coefficient  $\Gamma_{1111}$  has the form shown below:

$$\Gamma_{1111} = - \frac{\int_0^1 W'_1 W'_1 J_1(C1r) dr \int_0^1 W'_1 W'_1 J_1(C1r) dr}{(C1^2 - 1 + \nu^2) J_1^2(C1)}. \quad (15)$$

In Eq. (15),  $C1 = 1.463$  based on the Poisson’s ratio of the chosen Mylar diaphragm material and the coefficient  $\Gamma_{1111}$  assumes a negative value for the first mode. This means that system (14) would behave like an oscillator with a hardening cubic spring. Additionally, in Eq. (14),

$$\mu_1 = \int_0^1 \mu r W_1^2 dr, \quad f_1(t) = \int_0^1 r W_1 f(r, t) dr. \quad (16)$$

It should be pointed out that the effect of the nonlinearity depends on the strength of  $\varepsilon \Gamma_{1111}$  and the magnitude of  $\psi_1$ . Eq. (14) can be rewritten as

$$\ddot{\psi}_1 + 2\zeta \omega_1 \dot{\psi}_1 + \omega_1^2 \psi_1 - \varepsilon \Gamma_{1111} \psi_1^3 - f_1(t) = 0, \quad (17)$$

where  $\zeta = \varepsilon \mu_1 / \omega_1$ .

For a weakly nonlinear case and a resonance excitation close to the first natural frequency, as shown in Nayfeh and Mook [11], an analytical approximation can be obtained for the solution of Eq. (14). The frequency–response curve is given by

$$\left[ (\zeta \omega_1)^2 + \left( \sigma + \frac{3\Gamma_{1111}}{8\omega_1} \hat{a}^2 \right)^2 \varepsilon^2 \right] \hat{a}^2 = \frac{f_1^2}{4\omega_1^2}, \quad (18)$$

where  $\hat{a}$  is the response amplitude and the detuning parameter  $\sigma = (\omega - \omega_1)/\varepsilon$ .

In Fig. 4a and b, for the structure corresponding to Case 2 of Table 1 and the associated values shown in Table 2, the analytically predicted frequency–response curves are compared with the numerical results obtained by using the software AUTO97 [14,15]. The stable and unstable branches of the analytically predicted results generated by using Eq. (18) and equilibrium stability analysis are found to agree well with the numerical results obtained by using AUTO97 on the basis of Eq. (17). The numerical results obtained in the

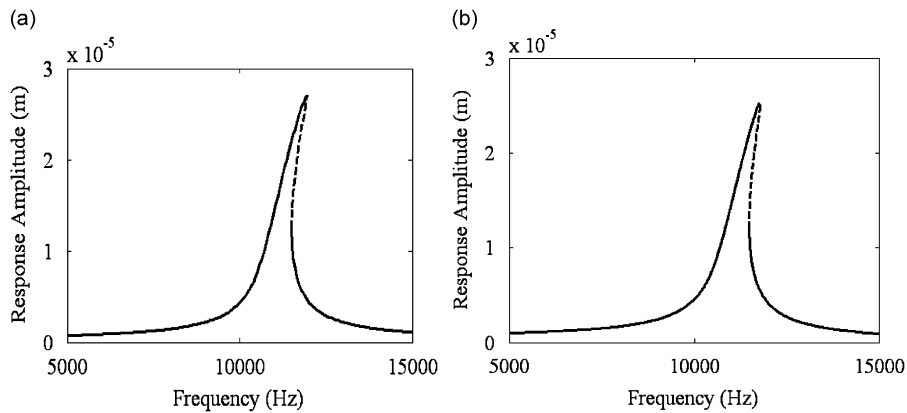


Fig. 4. Frequency–response curves for the diaphragm structure with  $k = 6.86$  and  $\zeta = 0.015$  when  $p = 60$  Pa: (a) analytical prediction results and (b) AUTO97 results. Stable and unstable branches of equilibrium solutions obtained from the analysis and AUTO97 are shown by using solid and dashed lines, respectively.

Table 2  
Dimensionless system parameters for the diaphragm structures of Table 1

Structure	$\varepsilon$	$\Gamma_{1111}$	$\varepsilon\Gamma_{1111}$	$\omega_1$
1	$5.2 \times 10^{-3}$	-58.54	-0.304	10.22
2	$1.3 \times 10^{-3}$	-49.7	-0.064	20.43
3	$8.15 \times 10^{-5}$	-39.82	-0.003	81.72

following sections have also been determined by using AUTO97. These results are used to illustrate the effects of initial tension and damping on the nonlinear response of the diaphragm.

### 3.1. Effects of initial tension on nonlinear response

As in the previous section, the three Mylar diaphragm structures presented in Table 1 are considered. It is recalled that the structural parameters and initial tension values are selected so that the first natural frequency in all three cases is 10.97 kHz. In Table 2, the numerical values of the dimensionless system parameters of Eq. (17) are provided for the three cases of Table 1.

First, analyses were conducted to investigate the nature of the frequency–response curves for different excitation pressure amplitudes with the initial tension  $k = 0$ . The results of these analyses are shown in Fig. 5a. When the excitation pressure level is quite low ( $p < 20$  Pa), the frequency–response curve is symmetric with respect to the natural frequency location and the diaphragm response resembles that of a linear oscillator. As the excitation pressure amplitude is increased to  $p = 60$  Pa, the frequency–response curves slightly bend to the right due to the cubic nonlinear term, showing a Duffing-oscillator-like behavior. For a higher excitation pressure level ( $p = 100$  Pa), the frequency–response curves not only bend to the right but also contain an unstable branch (dashed lines) and there is a frequency range in which multiple responses of the diaphragm can occur.

Next, for a fixed excitation pressure amplitude  $p = 60$  Pa, the frequency–response curves obtained for the three different diaphragm structures of Table 1 are compared in Fig. 5b. Similar to the behavior observed in the linear case, the response amplitude level increases with respect to increase in the tension level over the considered frequency range. These results indicate how the sensitivity can be enhanced by increasing the initial tension. Furthermore, although the frequency–response curves corresponding to  $k = 0$  do not have any unstable branches, as the tension parameter  $k$  is increased to  $k = 6.86$  and  $32.86$ , there are unstable branches. In each of these non-zero initial tension cases, there is a region of multiple responses in the vicinity of the first natural frequency. This indicates that the cubic nonlinearity effect gets stronger as  $k$  is increased, despite a decrease in  $|\varepsilon\Gamma_{1111}|$  (see Table 2). For  $k = 6.86$ , the turning points or saddle-node bifurcation points [14] are

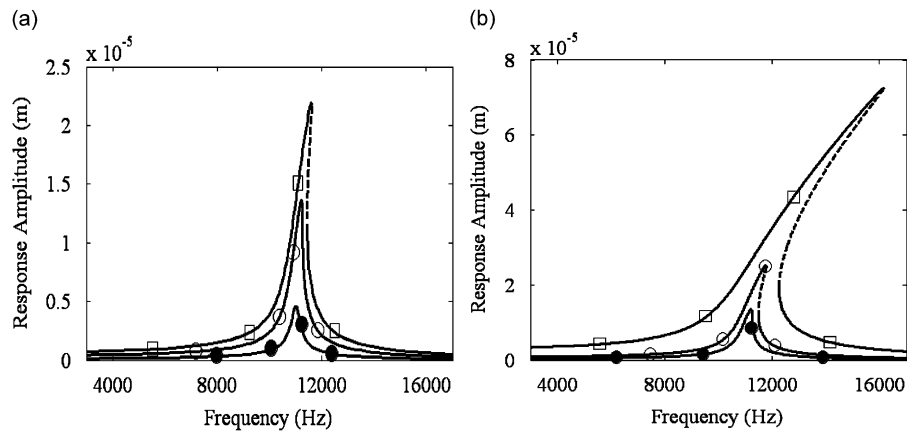


Fig. 5. Frequency–response curves obtained by using AUTO97; damping  $\zeta = 0.015$ : (a) for the diaphragm structure with  $k = 0$  and different excitation pressure levels, ( $\square$ ) for  $p = 100$  Pa, ( $\circ$ ) for  $p = 60$  Pa, and ( $\bullet$ ) for  $p = 20$  Pa, respectively; and (b) for different diaphragm structures of Table 1 when  $p = 60$  Pa, ( $\square$ ) for  $k = 32.86$ , ( $\circ$ ) for  $k = 6.86$ , and ( $\bullet$ ) for  $k = 0$ , respectively. Stable and unstable branches of equilibrium solutions are shown by using solid and dashed lines, respectively.

located at (11,491 Hz,  $1.26e-5$  m) and (11,784 Hz,  $2.50e-5$  m), and for  $k = 32.86$ , the turning points or saddle-node bifurcation points are located at (12,256 Hz,  $1.92e-5$  m) and (16,152 Hz,  $7.24e-5$  m). As the initial tension is increased, the turning points shift to higher frequency locations. These results indicate that although there is a trade-off between sensitivity and bandwidth, this can be addressed to a limited extent by decreasing the thickness and increasing the diaphragm tension parameter. Based on the results shown in Fig. 5b, it can be stated that as the tension is increased, the nonlinear effects are pronounced. Even for pressure measurements with  $p < 250$  Pa, the influence of the nonlinearity on the response of a thin diaphragm may be unacceptable. The present analyses illustrate the importance of carrying out a nonlinear analysis to design a pressure sensor with a thin diaphragm.

For an oscillator with a cubic nonlinearity, it is known that nonlinear responses can be prominent when the excitation frequency  $\omega$  is in the vicinity of the following [11]: (i) one-third of the first natural frequency, (ii) the natural frequency, and (iii) three times the natural frequency. Here, only the cases  $\omega \approx 1/3\omega_{01}$  and  $\omega_{01}$  are considered, since the sensor bandwidth is usually designed to be lower than the first natural frequency.

When the excitation frequency is close to one-third of the natural frequency ( $\omega/2\pi = 3665$  Hz), the variation of the diaphragm center response amplitude with respect to the excitation pressure level is shown in Fig. 6a, for the three different diaphragm structures of Table 1. In the considered pressure range of 0–3000 Pa, the response curves corresponding to  $k = 0$  and 6.86 are stable throughout the considered range. For “low” levels of the excitation pressure level, the nonlinear and linear responses are indistinguishable. However, as the excitation pressure level is increased, the nonlinear response curves obtained for the different initial tension values start deviating from the corresponding linear response curves and their slopes have lower values. In addition, for higher values of  $k$ , unstable branches are possible in the nonlinear case. This is illustrated for  $k = 32.86$  in Fig. 6a. For a pressure-sensor design, it is desirable that the sensor response be as “linear” as possible and free of instabilities such as those mentioned above.

To identify a region in Fig. 6a, where the response is close to being “linear”, an enlargement of the area labeled Z1 is considered in Fig. 6b. This region corresponds to low to moderate excitation pressure levels (0–500 Pa). For low to moderate values of  $k$  (say,  $0 \leq k \leq 6.86$ ), the nonlinear effects are weak and the nonlinear pressure response curves (solid lines) more or less coincide with the corresponding linear response curves ones (dotted lines). However, for  $k = 32.86$ , the pressure response curve is “linear”, only for excitation pressure levels below 100 Pa. These observations show that the cubic nonlinearity can limit the dynamic range of the sensor. To illustrate this effect, the variation of the maximum pressure level for which the response remains linear is shown with respect to the tension in Fig. 7. The different points at which the results have been numerically determined are shown along with the curve fit through these points. For a fixed sensor first natural frequency, as the initial tension is increased, the maximum pressure level for which the response remains linear

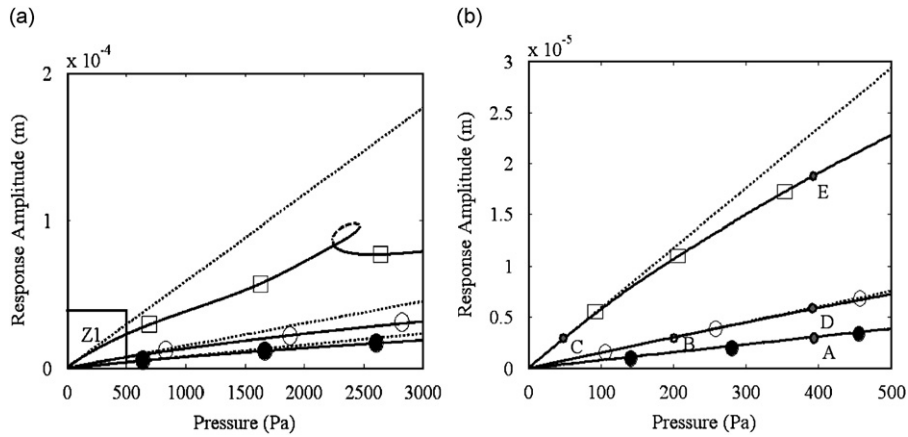


Fig. 6. Variation of the diaphragm response amplitude with respect to excitation pressure for damping  $\zeta = 0.015$ . The excitation frequency is fixed at  $\omega/2\pi = 3665$  Hz: (a) excitation pressure level from 0 to 3000 Pa and (b) enlargement of area Z1. In the linear case, the responses correspond to the straight lines with fine dots, and in the nonlinear case, the stable and unstable branches of equilibrium solutions are shown by using solid and dashed lines, respectively, ( $\square$ ) for  $k = 32.86$ , ( $\circ$ ) for  $k = 6.86$ , and ( $\bullet$ ) for  $k = 0$ , respectively. Spectral information of the responses at the locations marked A, B, C, D, and E are presented in Figs. 8 and 9.

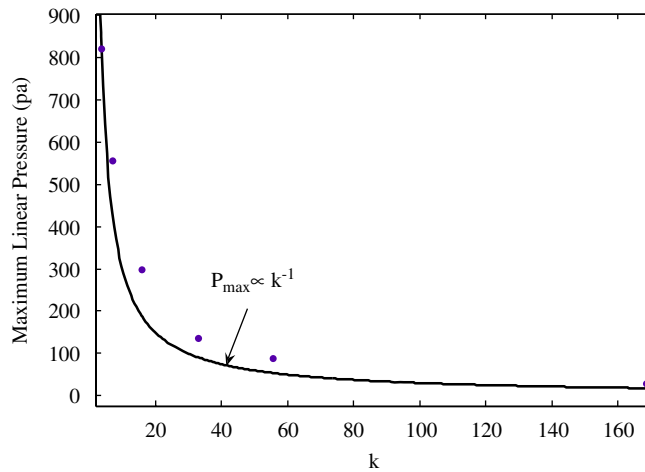


Fig. 7. Maximum pressure level for which the response is linear as a function of in-plane tension when the damping factor  $\zeta = 0.015$  and the excitation frequency is fixed at  $\omega/2\pi = 3665$  Hz.

decreases in magnitude. From a sensor design standpoint, it is desirable to have a sensor with a large dynamic range. However, this requires that the sensor diaphragm have low response amplitudes to keep nonlinear effects minimal, which in turn means a low sensitivity. This is another trade-off that one needs to consider in the design of pressure sensors.

To look into the nonlinear effects with respect to the excitation pressure level and the corresponding displacement response amplitude, two groups of test points are selected from Fig. 6. These groups of points are (A, B, C) and (A, D, E), where point A corresponds to  $k = 0$ , points B and D correspond to  $k = 6.86$ , and points C and E correspond to  $k = 32.86$ . The group (A, B, C) corresponds to the same response level and the group (A, D, E) corresponds to the same excitation level.

In Fig. 8, the steady-state time histories and the corresponding power spectral densities are shown for the responses associated with locations A, B, and C. The response amplitude is fixed at  $3.0 \times 10^{-6}$  m and the respective excitation pressure levels are 386 Pa for  $k = 0$ , 199 Pa for  $k = 6.86$ , and 51.2 Pa for  $k = 32.86$ . As shown in Fig. 8b, d, and e, in addition to the primary response at the excitation frequency that is close to one-third

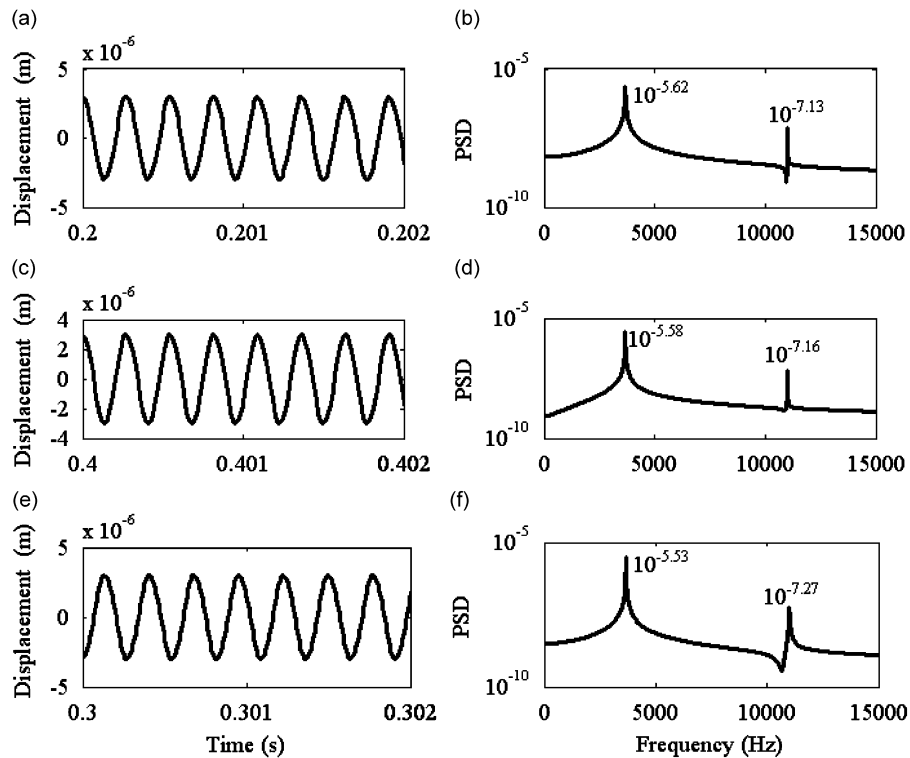


Fig. 8. Nonlinear response of diaphragm structure in time and frequency domains: (a) and (b) point A; (c) and (d) point B; and (e) and (f) point C.

of the first natural frequency, due to the effects of cubic nonlinearity, there is a secondary response at the third harmonic of the excitation frequency. The peak values at the excitation frequency and the corresponding third harmonic are also given in Fig. 8b, d, and f. It is noticed that the peak value of the third harmonic is about the same in all three cases with the same response amplitude. This indicates that for the diaphragm structures studied here, one needs to pay attention to the response amplitude rather than the nonlinear strength parameter  $|\varepsilon F_{1111}|$  to realize the allowable level of secondary harmonics in the sensor response.

Similarly, the steady-state time histories and the associated power spectral densities are shown in Fig. 9 for the responses corresponding to locations A, D, and E in Fig. 6. In this figure, the excitation pressure magnitude is fixed at 386 Pa for all three cases. As expected, the results corresponding to  $k = 32.86$  have the largest primary response as well as the largest third harmonic response. The ratio of  $10^{-0.86}$  between the peak value of the third harmonic response and that of the primary response for  $k = 32.86$  is larger than the ratio of  $10^{-1.51}$  obtained for  $k = 0$  and the ratio of  $10^{-1.19}$  obtained for  $k = 6.86$ . Due to the strong nonlinear effects, distortions can be observed in the time domain signal for  $k = 32.86$  (see Fig. 9d) and higher-order harmonics are discernible in the power spectrum density (see Fig. 9f). These results confirm again that the diaphragm structure with a higher initial tension can have a high sensitivity but suffer from strong nonlinear effects.

When the excitation frequency is close to the natural frequency, the response curves obtained for the three diaphragm structures are shown in Fig. 10. When one compares the results of Fig. 10 to those presented in Fig. 6, it can be seen that the linear response region and weakly nonlinear response region of the response curves of Fig. 10 are much shorter in range. This is due to the large response amplitudes observed during the primary resonance excitation. These results show that if the sensor bandwidth is extended to be somewhere close to the diaphragm's first natural frequency, the sensor dynamic range can be limited.

All the curves of Fig. 10 contain unstable branches (dashed lines). The turning points are located at (65.49 Pa,  $1.36e-5$  m) and (66.23 Pa,  $1.15e-5$  m) for  $k = 0$ , at (34.12 Pa,  $1.38e-5$  m) and (34.51 Pa,  $1.16e-5$  m) for  $k = 6.86$ , and at (8.93 Pa,  $1.39e-5$  m) and (9.04 Pa,  $1.19e-5$  m) for  $k = 32.86$ . For the diaphragm with larger  $k$ , instabilities occur at a lower pressure level. Although the turning points emerge at different excitation

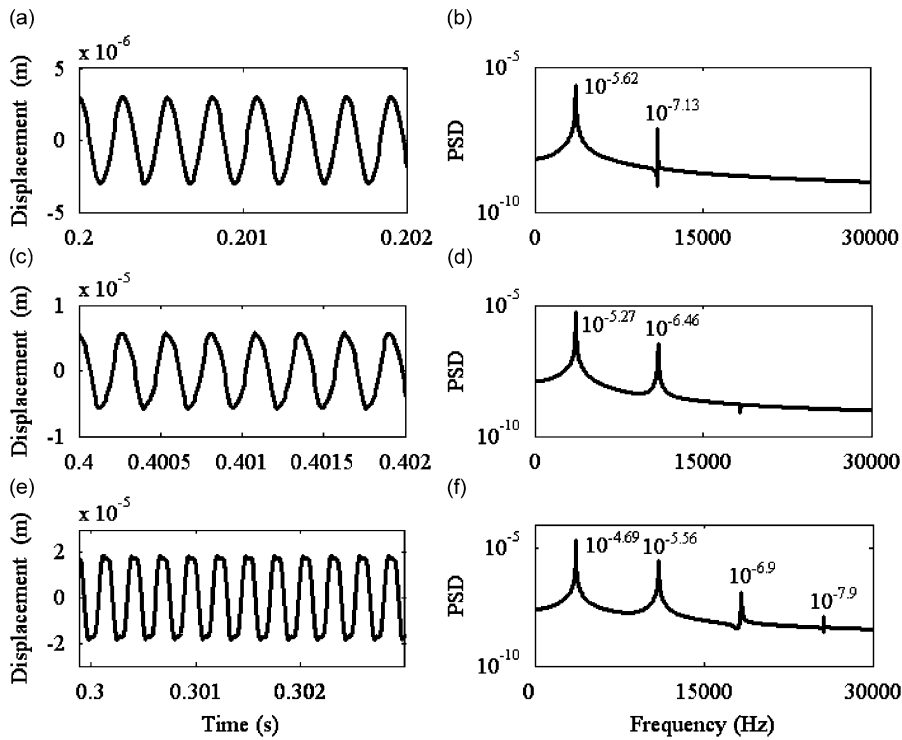


Fig. 9. Nonlinear response of diaphragm structure in time and frequency domains: (a) and (b) point A; (c) and (d) point D; and (e) and (f) point E.

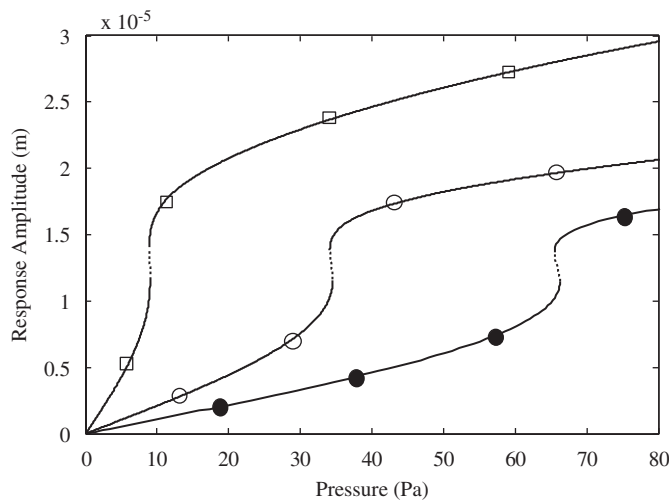


Fig. 10. Variation of the diaphragm response amplitude with respect to the excitation pressure for different diaphragm structures with the damping factor  $\zeta = 0.015$ , ( $\square$ ) for  $k = 32.86$ , ( $\circ$ ) for  $k = 6.86$ , and ( $\bullet$ ) for  $k = 0$ , respectively. The excitation frequency is fixed at  $\omega/2\pi = 11,300$  Hz. Stable and unstable branches of equilibrium solutions are shown by using solid and dashed lines, respectively.

pressure levels for each  $k$ , the corresponding response amplitudes at these turning points are almost the same. These results again point to the observation that the response amplitude level can be used to ascertain the influence of the nonlinearity.

In Fig. 11, the frequency–response curves are shown for diaphragm structures with the thickness  $h = 20 \mu\text{m}$ , the radius  $r = 1.75$  mm, and different levels of initial tension. In this figure, the dimensionless response

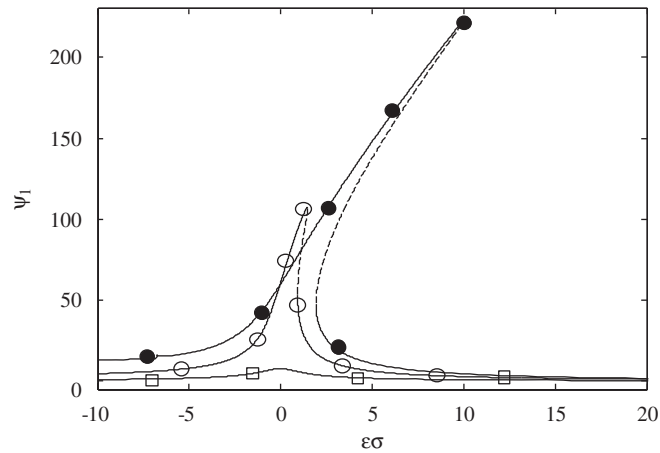


Fig 11. Frequency–response curve for the second diaphragm structure of Table 1 with different initial tension values and  $p = 60$  Pa, ( $\square$ ) for  $k = 32.86$ , ( $\circ$ ) for  $k = 6.86$ , and ( $\bullet$ ) for  $k = 0$ , respectively. Stable and unstable branches of equilibrium solutions are shown by using solid and dashed lines, respectively.

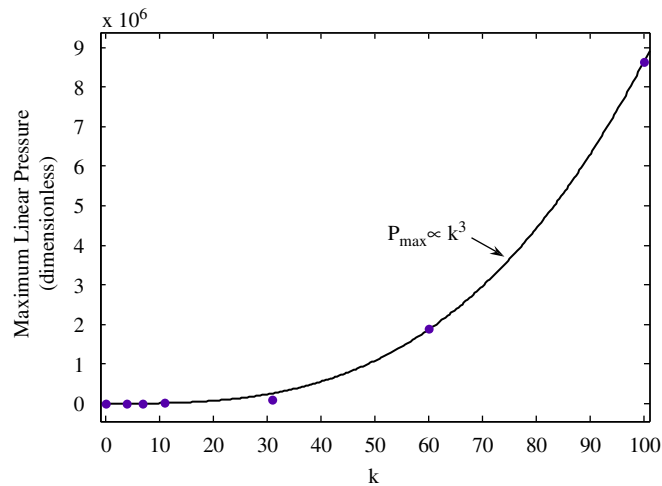


Fig 12. Maximum pressure level for which the response is linear as a function of in-plane tension, the damping factor  $\zeta = 0.015$  and the excitation frequency at  $\omega = 1/3\omega_1$ .

amplitude is plotted versus the dimensionless detuning parameter  $\varepsilon\sigma$ . It is clear that the frequency response corresponding to  $k = 0$  has a big bend to the right side and an unstable branch. As the tension parameter  $k$  is increased to 6.86, the bending is smaller and the unstable branch still exists. For  $k = 32.86$ , there are no unstable branches and the bending is not perceptible. Furthermore, as the tension level is increased, the response amplitude level decreases over the considered frequency range. These results indicate how the sensitivity can be reduced by increasing the initial tension. However, the dynamic range can be enhanced by increasing the initial tension. Similar to Fig. 7, the maximum pressure level for which the response remains linear is shown in Fig. 12 for different values of the initial tension. In this case, the maximum pressure level increases as  $k$  increases. This results agree well with the results presented in Ref. [9], where the static case was investigated.

### 3.2. Damping effects

In the earlier work of Yu and Balachandran [8], damping was found to be another determining factor in the sensor design. Based on linear analysis, it was ascertained that inclusion of damping can extend the flat region

of the diaphragm frequency–response curve so as to increase the sensor bandwidth. Since the response amplitude level is a key factor in determining the nonlinear effects, if sufficient damping can be included to attenuate the response at the first resonance, then it is expected that adding damping to the diaphragm structure can reduce the nonlinear effects.

For different damping levels, the frequency–response curves obtained for a diaphragm structure with  $k = 6.86$  and  $h = 20 \mu\text{m}$  are shown in Fig. 13 when the excitation pressure amplitude is held fixed at 200 Pa. With small damping ( $\zeta = 0.02$ ), there is an unstable branch (dashed lines) in the frequency–response curves. As the damping is increased to  $\zeta = 0.05$ , the unstable branch disappears and the response peak decreases considerably in magnitude. With sufficient damping ( $\zeta = 0.5$ ), the frequency–response curve becomes fairly flat and nonlinear effects can hardly be observed.

The variation of the response amplitude with respect to the excitation pressure amplitude is shown in Fig. 14 for the different diaphragm structures of Table 1, when the damping constant is held fixed at  $\zeta = 0.5$ . Note

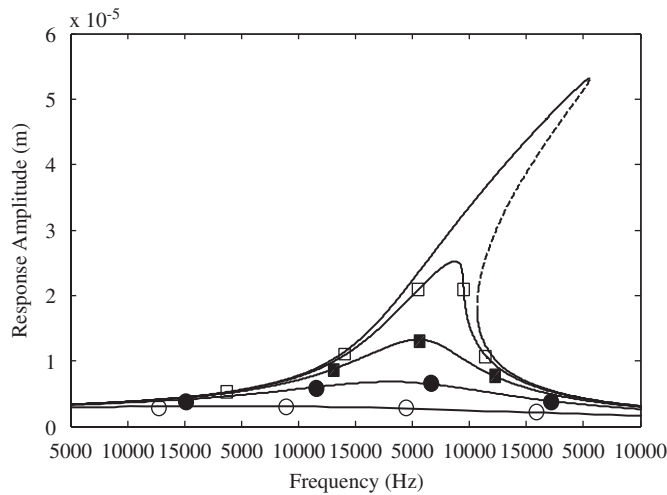


Fig 13. Frequency–response curves for diaphragm structure with  $k = 6.86$  and  $h = 20 \mu\text{m}$ . The excitation level is fixed at  $p = 200 \text{ Pa}$ . The line types are as follows: (i) (—) stable branch for  $\zeta = 0.02$  and (---) unstable branch for  $\zeta = 0.02$ ; (ii) (—□—) stable branch for  $\zeta = 0.05$ ; (iii) (—○—) stable branch for  $\zeta = 0.01$ ; (iv) (—●—) stable branch for  $\zeta = 0.2$ ; and (v) (—○—) stable branch for  $\zeta = 0.5$ .

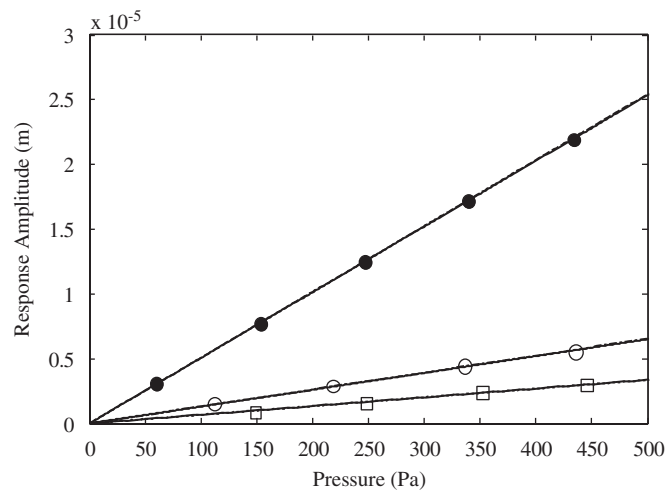


Fig 14. Variation of diaphragm response with respect to excitation pressure for the three diaphragm structures shown in Table 1 with damping factor  $\zeta = 0.5$ : (—●—) stable branch for  $k = 32.86$ ; (—○—) stable branch for  $k = 6.86$ ; and (—□—) stable branch for  $k = 0$ , respectively. The excitation frequency is fixed at  $\omega/2\pi = 11,300 \text{ Hz}$ .

that when pressure amplitude is in the range 0–500 Pa, all three structures exhibit fairly good linearity and the nonlinear response curves are coincident with those obtained from linear analysis. Compared with the results of Fig. 10, the dynamic range is dramatically increased when sufficient damping is added to a diaphragm.

In general, the damping can arise from the energy lost to a surrounding fluid and the energy dissipated internally within the diaphragm material. The first mechanism has been widely used for detuning the damping coefficient in the design of pressure sensors. For example, a perforated backplate has been included in many condenser microphones to increase damping. As shown here, such inclusions can not only enhance the bandwidth of a pressure sensor but also improve its dynamic range without loss of sensitivity.

#### 4. Concluding remarks

In this article, a pressure-sensor diaphragm model based on a plate with in-plate tension is presented. Earlier linear analysis of this model showed that the dynamic behavior of the diaphragm exhibits a transition from plate behavior to membrane behavior, when the tension parameter  $k$  is between 1 and 20 with the plate behavior dominating for  $k < 1$  and the membrane behavior dominating for  $k > 20$ . From the linear analyses and results, it was inferred that for a given diaphragm radius, one can realize the desired high sensitivity and high bandwidth by decreasing the diaphragm thickness and applying an appropriate tension. This was believed to be a solution to address the trade-off between the sensitivity and bandwidth and a useful guideline to design a high performance sensor for dynamic pressure sensing. However, when the analysis is extended to the nonlinear regime, such a solution is seen to fail, since a high sensitivity is seen to be accompanied by strong nonlinear effects that reduce the sensor dynamic range. Within the scope of the sensor bandwidth, nonlinear effects are pronounced when the excitation frequency is close to either one-third of the first natural frequency or the natural frequency. As illustrated by the nonlinear analysis and accompanying results obtained, nonlinear effects can be present even during low to moderate excitation pressure levels and the nonlinear effects become stronger when the in-plane tension is increased and diaphragm thickness is decreased. Furthermore, it is noticed that the response amplitude of the diaphragm is the dominant factor that determines the strength of nonlinearity.

It is suggested that inclusion of damping can not only be used to enhance the sensor bandwidth, but also be considered as a potential solution to address the trade-off between sensitivity and dynamic range of the pressure sensor, since damping can be effective in reducing the nonlinear effects. Careful choices of the tension parameter and damping coefficient, two important parameters in the design of pressure sensors, can enable the realization of high-performance pressure sensors for various applications.

#### Acknowledgments

The first author acknowledges support received from the US National Science Foundation through Award no. CMMI 0644914, and the second author acknowledges support received from MST of PRC under 973 Grant 2005CB724101.

#### Appendix A. Stress function and related details

For completeness, additional details corresponding to the stress function used in Eqs. (2)–(6) are provided here. Starting from Love's equations [11–13], including damping and the transverse loading per unit area  $f(r, \theta; t)$ , the nonlinear partial-differential equation governing a plate with initial tension can be obtained as

$$\rho h \frac{\partial^2 w}{\partial t^2} + D \nabla^4 w = \tilde{N}_r \frac{\partial^2 w}{\partial r^2} + \tilde{N}_\theta \left( \frac{1}{r} \frac{\partial w}{\partial r} + \frac{1}{r^2} \frac{\partial^2 w}{\partial \theta^2} \right) + 2N_{r\theta} \left( \frac{1}{r} \frac{\partial^2 w}{\partial r \partial \theta} - \frac{1}{r^2} \frac{\partial w}{\partial \theta} \right) - 2\mu \frac{\partial w}{\partial t} + f(r, \theta; t), \quad (\text{A.1})$$

where  $r$  is the radial distance from the center,  $\theta$  is the angular coordinate,  $w(r, \theta; t)$  is the transverse displacement,  $\mu$  is the damping coefficient, and  $f(r, \theta; t)$  is the transverse loading per unit area. Let

$$\tilde{N}_r = N_0 + N_r, \quad (\text{A.2})$$

$$\tilde{N}_\theta = N_0 + N_\theta, \tag{A.3}$$

where  $N_0$  is the initial tension per unit length. Neglecting the in-plane inertia, one has

$$\frac{\partial N_r}{\partial r} + \frac{1}{r} \frac{\partial N_{r\theta}}{\partial \theta} + \frac{N_r - N_\theta}{r} = 0, \tag{A.4}$$

$$\frac{\partial N_{r\theta}}{\partial r} + \frac{1}{r} \frac{\partial N_\theta}{\partial \theta} + \frac{2N_{r\theta}}{r} = 0. \tag{A.5}$$

To determine  $N_r$  and  $N_\theta$ , a stress function  $\Phi(r,\theta,t)$  that satisfies Eqs. (A.4) and (A.5) is introduced and defined by

$$N_r = \frac{1}{r} \frac{\partial \Phi}{\partial r} + \frac{1}{r^2} \frac{\partial^2 \Phi}{\partial \theta^2}, \tag{A.6}$$

$$N_\theta = \frac{\partial^2 \Phi}{\partial r^2}, \tag{A.7}$$

$$N_{r\theta} = -\frac{1}{r} \frac{\partial^2 \Phi}{\partial r \partial \theta} + \frac{1}{r^2} \frac{\partial \Phi}{\partial \theta}. \tag{A.8}$$

After substituting Eqs. (A.6)–(A.8) into Eqs. (A.2) and (A.3) and then into Eq. (A.1), the equation of motion governing a circular plate can be written as given by Eq. (2). It is also mentioned that for Hookean isotropic material, the in-plane forces can be written in terms of the mid-plane strains

$$\tilde{N}_r = \frac{Eh}{1-\nu^2} (e_r + \nu e_\theta), \tag{A.9}$$

$$\tilde{N}_\theta = \frac{Eh}{1-\nu^2} (\nu e_r + e_\theta), \tag{A.10}$$

$$N_{r\theta} = \frac{Eh}{2(1+\nu)} e_{r\theta}. \tag{A.11}$$

Combining Eqs. (A.6)–(A.11), one can obtain

$$e_r = \frac{1}{Eh} \left( \frac{1}{r} \frac{\partial \Phi}{\partial r} + \frac{1}{r^2} \frac{\partial^2 \Phi}{\partial \theta^2} - \nu \frac{\partial^2 \Phi}{\partial r^2} \right) + \frac{1-\nu}{Eh} N_0, \tag{A.12}$$

$$e_\theta = \frac{1}{Eh} \left[ \frac{\partial^2 \Phi}{\partial r^2} - \nu \left( \frac{1}{r} \frac{\partial \Phi}{\partial r} + \frac{1}{r^2} \frac{\partial^2 \Phi}{\partial \theta^2} \right) \right] + \frac{1-\nu}{Eh} N_0, \tag{A.13}$$

$$e_{r\theta} = \frac{2(1+\nu)}{Eh} \left( \frac{1}{r^2} \frac{\partial \Phi}{\partial \theta} - \frac{1}{r} \frac{\partial^2 \Phi}{\partial r \partial \theta} \right). \tag{A.14}$$

The mid-plane strains can also be written in terms of the transverse displacement  $w$ , the radial displacement  $u$ , and the hoop displacement  $v_h$  as

$$e_r = \frac{\partial u}{\partial r} + \frac{1}{2} \left( \frac{\partial w}{\partial r} \right)^2, \tag{A.15}$$

$$e_\theta = \frac{u}{r} + \frac{1}{r} \frac{\partial v_h}{\partial \theta} + \frac{1}{2r^2} \left( \frac{\partial w}{\partial \theta} \right)^2, \tag{A.16}$$

$$e_{r\theta} = \frac{1}{r} \frac{\partial u}{\partial \theta} + \frac{\partial v_h}{\partial r} - \frac{v_h}{r} + \frac{1}{r} \frac{\partial w}{\partial r} \frac{\partial w}{\partial \theta}. \tag{A.17}$$

## References

- [1] Y. Matsuoka, Y. Yamamoto, M. Tanabe, S. Shimada, K. Yamada, A. Yaskuwa, H. Matsuzaka, Low-pressure measurement limits for silicon piezoresistive circular diaphragm sensors, *Journal of Micromechanics and Microengineering* 5 (1995) 32–35.
- [2] M. Pedersen, M.G.H. Meijerink, W. Olthuis, P. Bergveld, A capacitive differential pressure sensor with polyimide diaphragm, *Journal of Micromechanics and Microengineering* 7 (1997) 250–252.
- [3] N. Zeng, C. Shi, D. Wang, M. Zhang, Y. Liao, Diaphragm-type fiber-optic interferometric acoustic sensor, *Optical Engineering* 42 (2003) 2558–2562.
- [4] D. Kouzoudis, G.A. Grimes, The frequency response of magnetoelastic sensors to stress and atmospheric pressure, *Smart Materials and Structures* 9 (2000) 1–5.
- [5] M. Yu, Fiber-Optic Sensor Systems for Acoustic Measurements, PhD Dissertation, University of Maryland, College Park, MD, 2002.
- [6] M. Yu, B. Balachandran, Acoustic measurements using a fiber optic sensor system, *Journal of Intelligent Material Systems and Structures* 14 (2003) 409–414.
- [7] E.S. Olson, Observing middle and inner ear mechanics with novel intracochlear pressure sensors, *Journal of the Acoustical Society of America* 103 (1998) 3445–3463.
- [8] M. Yu, B. Balachandran, Sensor diaphragm under initial tension: linear analysis, *Experimental Mechanics* 45 (2005) 123–129.
- [9] M. Sheplak, J. Dugundji, Large deflections of clamped circular plates under initial tension and transitions to membrane behavior, *ASME Journal of Applied Mechanics* 65 (1998) 107–115.
- [10] Y.H. Zhou, An analysis of pressure–frequency characteristics of vibrating string-type pressure sensor, *International Journal of Solids and Structures* 38 (2001) 7101–7111.
- [11] A.H. Nayfeh, D.T. Mook, *Nonlinear Oscillations*, Wiley, New York, 1979.
- [12] A.H. Nayfeh, P.F. Pai, *Linear and Nonlinear Structural Mechanics*, Wiley, New York, 2004.
- [13] W. Soedel, *Vibrations of Shells and Plates*, Marcel Dekker, New York, 1993.
- [14] A.H. Nayfeh, B. Balachandran, *Applied Nonlinear Dynamics: Analytical, Computational, and Experimental Methods*, Wiley, New York, 1995.
- [15] E.J. Doedel, A.R. Champneys, T.F. Fairgrieve, Y.A. Kuznetsov, B. Sandstede, X. Wang, *AUTO97: Continuation and Bifurcation Software for Ordinary Differential Equations (with HOMCONT)*, Technical Report, Concordia University, 1997.